Volume 18
Number 19
7 October 2025
Pages 8715–8980

Energy & Environmental Science

rsc.li/ees

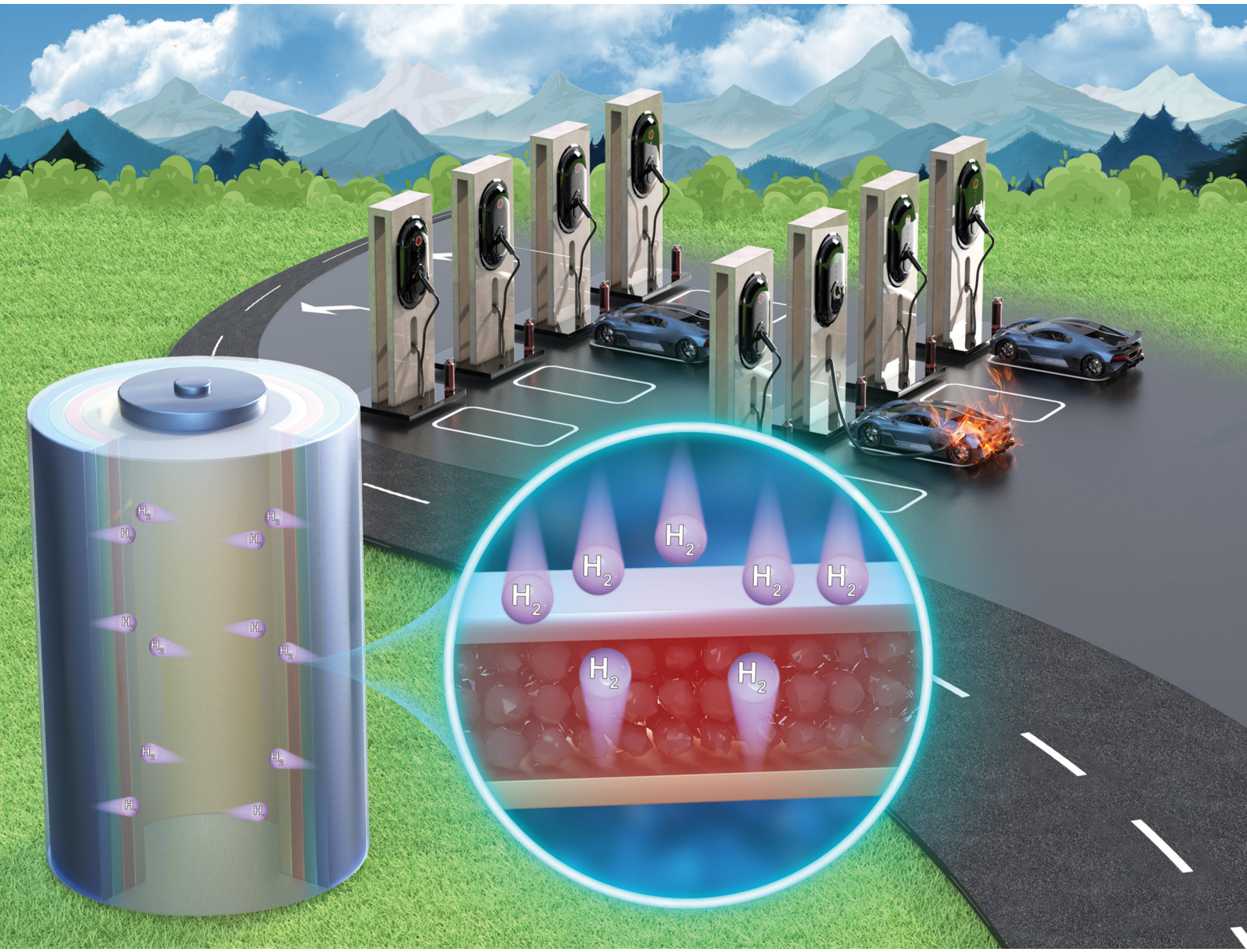

ISSN 1754-5706

ROYAL SOCIETY OF CHEMISTRY

PAPER
Guoming Ma, Dingguo Xia, Hao Zhao *et al.*
Operando observing hydrogen evolution in commercial lithium-ion batteries

Energy & Environmental Science

ROYAL SOCIETY OF CHEMISTRY

PAPER

View Article Online
View Journal | View Issue

Cite this: *Energy Environ. Sci.*, 2025, **18**, 8756

Operando observing hydrogen evolution in commercial lithium-ion batteries†

Yuan Wang,‡[a] Shuyan Guo,‡[a] Yuntian Guo,[ab] Peng Zhang,[c] Guoming Ma,*[b] Dingguo Xia *[d] and Hao Zhao *[a]

Received 28th May 2025,
Accepted 14th July 2025

DOI: 10.1039/d5ee02940f

rsc.li/ees

Operando monitoring of the H_2 evolution within lithium-ion batteries is essential for decoding their thermal runaway mechanism and preventing fires. Here, we track the H_2 evolution over multiple charging–discharging cycles of commercial 18 650 batteries *via* an *operando* surface-modified fiber Bragg grating sensor. Time-resolved reversible adsorption–desorption and irreversible formation of H_2 are discovered to be associated with the temperature inside batteries. Notably, we experimentally observe unique negative temperature coefficient (NTC) behaviour for the H_2 evolution, in which H_2 concentration inversely changes with the internal temperature above a critical temperature. Further numerical and analytical analyses reveal the H_2 evolution mechanism through Fickian diffusion and Soret diffusion, indicating the NTC behaviour can mitigate the severe hazards of thermal runaway. This work has key value for advancing the design of next-generation high-safety batteries.

Broader context

Frequent safety accidents involving lithium-ion battery energy storage systems worldwide have drawn significant industry attention, such as the two explosion accidents of the Xiaomi SU7 electric vehicle and the large-scale fire at the Moss Landing energy storage station in California, USA. These accidents have not only resulted in substantial casualties and property damage, but have also sparked profound market skepticism regarding the safety of lithium battery technologies. Therefore, there is an urgent need for a comprehensive understanding of their thermal runway mechanism including internal flammable gases. In particular, hydrogen (H_2) is the dominant gas produced during thermal runaway, with concentrations of up to 70%, and serves as the principal contributor to combustion and explosion due to its high flame propagation speed and broad explosion limits. Our study addresses the long-standing puzzle of H_2 evolution mechanism in commercial lithium-ion batteries *via* an *operando* surface-modified fiber Bragg grating sensor and for the first time reveals the reversible adsorption/desorption and irreversible formation of H_2. In particular, a unique negative temperature coefficient (NTC) behaviour of the H_2 evolution is first discovered in experiments. The findings are essential for understanding the thermal runaway of lithium-ion batteries and providing new safety-oriented battery design strategies for improving their reliability.

Introduction

Lithium-ion batteries play a critical role in sustainable energy storage and conversion. They are widely applied in various scenarios such as in electric vehicles, aircraft, power grids, and portable electronics.[1–3] However, in recent years, frequent explosion and fire accidents in energy storage facilities, electric vehicles, and battery manufacturing plants have led to casualties, substantial economic losses, and severe anxiety toward battery utilization. Particularly for next-generation high-energy-density batteries in long-range electrical vehicles, low-altitude aircraft and electrically driven vessels, the risk of thermal runaway events raises critical safety concerns for the limited escape timing. Thermal runaway originates from the temperature rise inside batteries to beyond the safe operating range, which often initiates a series of exothermal reactions between flammable gases and the electrolytes. These reactions further lead to a rapid increase in temperature, electrolyte oxidation, and even fires.[4–6] In particular, H_2 is the dominant species and accounts for up to 70%[7] of the released gases within a lithium iron phosphate (LFP, $LiFePO_4$) battery. It serves as the major

[a] *School of Mechanics and Engineering Science, Peking University, Beijing, 100871, P. R. China. E-mail: h.zhao@pku.edu.cn*
[b] *State Key Laboratory of Alternate Electrical Power System with Renewable Energy Sources, North China Electric Power University, Beijing, 102206, P. R. China. E-mail: ncepumgm@ncepu.edu.cn*
[c] *Department of Mechanical Engineering, City University of Hong Kong, Kowloon, 999077, Hong Kong, P. R. China*
[d] *Beijing Key Laboratory of Theory and Technology for Advanced Batteries Materials, School of Materials Science and Engineering, Peking University, Beijing, 100871, P. R. China. E-mail: dgxia@pku.edu.cn*

† Electronic supplementary information (ESI) available: Materials and methods, supplementary text 1 and 2, Fig. S1–S17, Tables S1–S5 and ref. S1–S10. See DOI: https://doi.org/10.1039/d5ee02940f

‡ These authors contributed equally to this work.

contributor to these battery fire accidents due to having the broadest explosion limit and highest flame propagation speed among flammable gases.[8] It is also observed that H_2 exhibits potential interactions with cathode materials with substantial heat release and strong correlation with cathode degradation and solid electrolyte interface (SEI) decomposition.[6] The decomposition of the unstable SEI at elevated temperatures exacerbates the accumulation of dead lithium and continuous electrolyte decomposition, thereby increasing gas evolution and potentially leading to H_2 accumulation.[9,10] Therefore, we now must gain a comprehensive understanding of the thermal runway mechanism hinging on the quantitative H_2 evolution within a battery for early warning and mitigation of battery fires.

Quantification of the gas evolution in batteries has been reported in numerous studies. However, this quantification has mainly relied on *ex situ* approaches such as gas chromatography-mass spectrometry (GC-MS)[11,12] or on *in situ* approaches such as online/differential electrochemical mass spectrometry (O/DEMS)[13,14] and Fourier transform infrared spectroscopy (FT-IR),[15,16] which possess relatively low temporal resolution for gas quantification. Moreover, as these destructive sampling methods involve either collection of the battery gases or flow of carrier diluents through the battery gases, the battery under sampling deviates from its normal operation conditions. It results in changes both in the electrolyte composition and gas concentration, and further triggers a series of secondary parasitic reactions and alters their reaction equilibrium.[17] Quantification of the gas evolution inside an intact battery under normal operation conditions is very difficult. Thus, advancements in implantable and non-destructive sensors that enable *operando* gas monitoring with excellent temporal resolution are urgently needed.

An ideal non-destructive solution for *operando* monitoring of battery characteristics, such as temperature, stress, and pressure, is the use of optical fibre sensors due to their compact size (diameter ~125 μm), high sensitivity, prompt response, and immunity to electromagnetic interference.[18–20] Pinto and coworkers first used optical fiber sensors to monitor the temperature inside a battery.[21] Tarascon's group quantified the heat release and explored SEI formation by directly measuring the internal temperature and pressure of batteries *via* fiber Bragg grating (FBG) sensors.[22] Recently, Wang's group observed the correlation between thermal runaway and the internal temperature/pressure of batteries by inserting a multifunctional optical fiber sensor into a 18 650 lithium-ion battery.[23] Moreover, several studies have investigated electrolyte/electrode interface characteristics, such as the turbidity of electrolytes and the functional groups of C═C and C═O bonds, by using tilted FBG sensors,[24–26] hollow-core fiber sensors,[27] and infrared fiber evanescent wave spectroscopy.[28,29] However, it is seen from the literature above that *in situ* non-destructive quantification of the gaseous components during battery cycling has yet to be achieved. Direct observations of the H_2 evolution and interactions with electrodes and electrolytes under normal cycling operation are lacking because of the complex thermochemical couplings and limited diagnostic approaches.

To reveal the H_2 evolution in lithium-ion batteries, we developed a surface-modified FBG sensor and embedded it into the central void of a battery for simultaneous measurements of the internal temperature and transient H_2 evolution under normal operation conditions. Cylindrical batteries (*e.g.*, common models like 18 650, 21 700 and 4680) have become an ideal choice for highly reliable applications thanks to their robust structure and excellent thermal dissipation. Despite this, there remain devastating thermal runaway issues with cylindrical batteries. Hence, we select commonly used commercial 18 650 batteries as a typical example to study the H_2 evolution during the charging–discharging cycles. This work is the first to directly quantify the H_2 evolution within an intact battery. The battery underwent multiple charging–discharging cycles at different C rates, and the time-resolved data of H_2 concentration were collected. Moreover, we discovered novel negative temperature coefficient (NTC) behaviour in H_2 during normal charging–discharging cycles, in which the H_2 concentration inversely changes with the temperature inside the battery above a critical temperature, which is dependent on the battery structure and charging–discharging conditions. The NTC behaviour is highly associated with the H_2 evolution within a battery and potentially helps to suppress the occurrence of thermal runaway. Furthermore, we successfully predicted the H_2 evolution mechanism, including the NTC behaviour, through calculations by introducing Soret diffusion[30] of H_2 to the governing equations[31] to establish a numerical model of the H_2 evolution between the anode and electrolyte. Therefore, the present work provides a comprehensive understanding of the mechanism of H_2 evolution and new insights into the battery degradation and thermal runaway. Moreover, the present H_2 evolution theory has also been validated for LFP thermal runaway and for high-energy-density battery cycles in numerical simulations, where the H_2 growth could be highly inhibited with the inclusion of NTC behaviour. We further provide crucial theoretical guidance to amplify the NTC behaviour by optimizing the operation strategy in a high Joule heating rate and the design of high-energy-density batteries in terms of electrolytes and anodes.

Results and discussion

Principle of the FBG sensing technique

We first examined the performance of the *operando* FBG sensors in quantifying the H_2 evolution in lithium-ion batteries through a series of calibrations involving temperature changes, H_2 concentration changes, and battery cycling at different C rates. Fig. 1A (upper left) shows the configuration and basic sensing principle of an FBG sensor inscribed in a single-mode optical fiber with a uniform diameter of 125 μm. The FBG can be considered an optical reflector with a specific narrow resonance (Bragg resonance λ_B), $\lambda_B = 2n_{eff}\Lambda$, where n_{eff} is the effective refractive index of the grating and Λ is the period of the Bragg grating. Variations in environmental parameters, such as temperature or strain, around the FBG sensor cause fluctuations in both n_{eff} and Λ, thereby leading to a shift in the central wavelength ($\Delta\lambda_B$).[32,33] However, the unprocessed bare FBG cannot be directly utilized for H_2 quantification, as it is

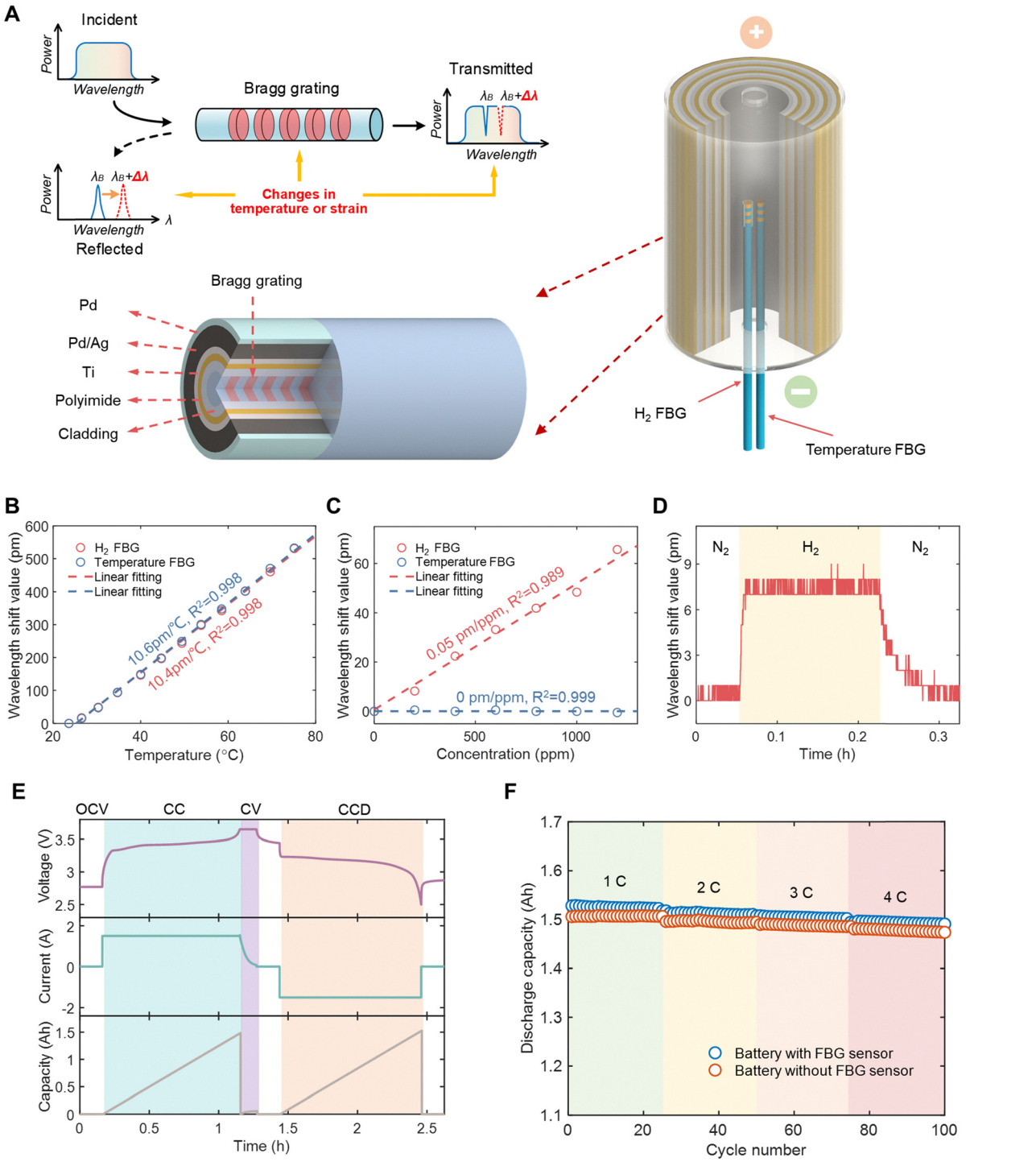

Fig. 1 Concept of FBG sensing inside a battery and evaluation of the battery performance with the FBG sensor. (A) Basic principle of the FBG sensor (upper left) together with the configuration of the H_2 FBG sensor used in this work (lower left) and the concept of an FBG sensor placed inside an 18 650 cylindrical battery (right). (B) Wavelength responses of the sensors to temperature over the range of 25 to 75 °C, in which the temperature FBG sensor and the H_2 FBG sensor both show linear responses. (C) Wavelength responses of the sensors to H_2 over the range of 0 to 1200 ppm. The H_2 FBG sensor exhibits a linear response within this range, whereas the temperature FBG sensor is insensitive to H_2. (D) Temporal resolution characteristics of the H_2 FBG sensor to the H_2. (E) Demonstration of the charging–discharging strategy of the battery when the C rate is set as 1C. The charging–discharging cycles were performed in the following steps: a constant-current (CC) charging was carried out until the voltage reached 3.65 V, followed by a constant-voltage (CV) charging with a cut-off current of 0.05C. This was followed by a period of 10-minute open-circuit voltage (OCV), and finally, a constant-current discharging (CCD) was performed until the voltage dropped to 2.5 V, with another 10-minute OCV period. The duration for each OCV step is 10 minutes. (F) The battery lifetime performance is unaffected by implantation of the FBG sensor. The battery was continuously operated at different C rates (1C, 2C, 3C and 4C) for a total of 100 cycles at ambient temperature, with each C rate fixed for 25 cycles.

insensitive to the H_2 concentration. We solved this problem by coating H_2-sensitive materials on the surface of the bare FBG, as described in the Methods section. Several layers were coated on the fiber cladding in the Bragg grating area (Fig. 1A, lower left): a polyimide layer (1 μm), a titanium (Ti) layer (20 nm), a palladium/silver (Pd/Ag) composite layer (400 nm), and a Pd layer (160 nm). Functioning as H_2-sensitive materials, the Pd and Pd/Ag layers expand in size after absorbing H_2 (Fig. S1A, ESI†),[34–36] causing strain variations on the FBG surface, so as to make the sensor sensitive to the H_2 concentration. Both the polyimide layer and the Ti layer serve as adhesives to prevent the outer coating from delamination.

We selected the widely used LFP battery for investigation.[37] To track the internal temperature and H_2 evolution within a battery, both a temperature FBG sensor (bare FBG) and a H_2 FBG sensor were implanted in a commercial 18 650 LFP battery, with the battery specifications given in Table S1 (ESI†) (the surface morphology and elemental composition of LFP are shown in Fig. S2 and S3, ESI†). The FBG sensor is suspended in the central void (diameter ~2 mm) of the jelly roll of the 18 650 LFP battery and is parallel to its axis (see Fig. 1A, right), effectively eliminating additional strain on the FBG sensor. The details of the implantation process are provided in both the Methods section and Fig. S4 (ESI†).

Fig. 1B and C show the wavelength responses of the temperature FBG sensor and the H_2 FBG sensor to changes in both the temperature and H_2 concentration. Both sensors demonstrate linear responses (R^2 = 99.8%) to temperature changes, with almost the same sensitivity coefficient (k_T) of 10.5 ± 0.1 pm $^\circ C^{-1}$. However, the H_2 FBG sensor has a high sensitivity (k_{H_2}) of 0.05 pm ppm^{-1} to changes in the H_2 concentration, whereas the temperature FBG sensor is insensitive to H_2. The response time of the H_2 FBG sensor to H_2 is about 15 s, which exhibits an excellent temporal resolution (Fig. 1D). Also, the H_2 FBG sensor generally shows minimal interference from other non-H_2 indicator gases (Fig. S5, ESI†), demonstrating excellent selectivity and negligible cross-interference capability. Furthermore, both sensors are insensitive to the surrounding pressure (Fig. S6, ESI†), which rules out the interference of the internal pressure within batteries during the charging–discharging cycles. We additionally verified that, with the sensor arranged as described above, there is negligible temperature gradient between the two sensors, and they exhibit identical temperature responses (Fig. S7, ESI†). Therefore, the temperature (ΔT) and H_2 concentration (ΔC) changes can be synchronously determined by monitoring the central wavelength shifts of both sensors ($\Delta\lambda_{B,T}$ and $\Delta\lambda_{B,H_2}$; see the Methods section).

After the above sensing calibration, we evaluated the impact of FBG sensor implantation on the electrochemical characteristics and cyclability of the battery. Fig. 1E depicts the charging–discharging protocol within one cycle used in the present study, taking 1C as an example (where 'C' denotes the ratio of the charge/discharge current to the rated capacity). The absence of voltage distortion or internal short circuits during cycling (Fig. S8, ESI†) reveals that the implanted FBG sensor has little effect on the internal insulation of the battery. Furthermore, Fig. 1F shows that there is only a 2.4% decrease in the capacity of the battery with the FBG sensor compared with that of a fresh battery for at least 100 cycles at different C rates (1C to 4C; these C rates are commonly applied during battery operation).

After the above experiments were completed, the battery was disassembled, and the H_2 FBG sensor was observed *via* scanning electron microscopy (SEM). The Pd layer is still uniformly coated on the H_2 FBG surface (Fig. S9, ESI†), indicating excellent long-term reliability of the H_2 FBG sensor under different charging–discharging conditions. The above results demonstrate that the influence of the implanted FBG sensor on the battery performance is negligible and that the FBG sensor enables non-destructive *operando* quantification of both the temperature and H_2 concentration within batteries.

Reversible evolution and irreversible formation of H_2 inside the battery

After verifying the performance of the H_2 FBG sensor, it was subsequently employed to determine the H_2 evolution within the battery. The experimental setup for quantifying multiple parameters within a battery is depicted in Fig. S10 (ESI†). The battery underwent 40 charging–discharging cycles from 1C to 4C (10 cycles for each C rate) to analyse the H_2 evolution kinetics under different C rates. The synchronous optical responses of both the temperature and H_2 FBG sensors indicate that the sensors can quickly respond to voltage changes (Fig. S11, ESI†). The influence of temperature on the H_2 FBG sensor was evaluated in a separately designed experiment (see the Methods section and Fig. S12, ESI†). The results confirm that the H_2 concentration measured within the battery by the H_2 FBG sensor is not affected by background fluctuations in the temperature within the battery.

The time-resolved internal temperature (T, Fig. 2A, top) and H_2 concentration in the central void of the jelly roll (C_{H_2}, Fig. 2A, bottom) over the 40 cycles were decoupled and extracted from the wavelength shift data ($\Delta\lambda_B$) acquired in *operando* mode. The temperature and H_2 concentration at specific charging–discharging stages in one cycle (1C as an example) are plotted in Fig. 2B for a clearer view of the FBG responses. Fig. 2A and B show that the H_2 concentration periodically changes during the operation cycle, *i.e.*, increases in the CC, CV, and CCD stages, while decreases in the open-circuit stage. In particular, the concentration reaches a maximum when the temperature peaks and almost returns to the initial level after the battery cools down. This result clearly reveals the temperature-dependent reversible evolution of H_2 within the battery during the charging–discharging cycle. H_2 formation from the chemical interactions between electrodes and electrolytes is generally irreversible, and the H_2 concentration in this case is unlikely to return to the initial level.[12,38] Therefore, the reversible evolution of H_2 within the battery is highly likely due to its physical adsorption/desorption on/from the anode material (graphite).[39,40]

To examine the potential for physical adsorption/desorption on/from the anode material, we further quantified the surface

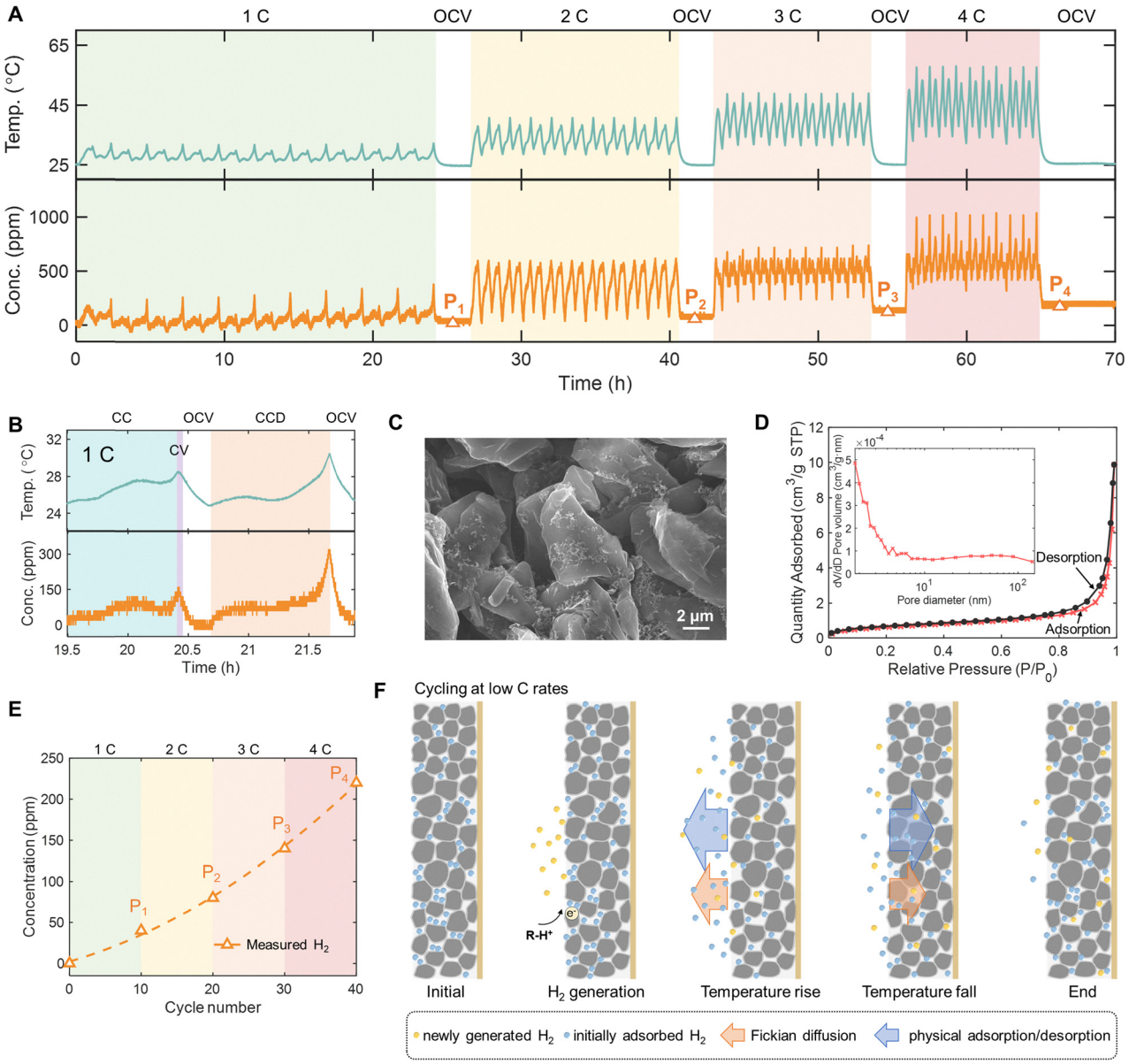

Fig. 2 *Operando* probed temperature and H_2 evolution kinetics inside 18 650 batteries. (A) Time-resolved internal temperature (green line) and internal H_2 concentration (orange line) evolutions during long-term cycling. A 2.5-hour cooling period is set between charging–discharging cycles at different C rates to ensure that the internal temperature returns to the ambient temperature. (B) Relationship between the time-resolved response and cycling stage, taking a 1C charging–discharging cycle captured from long-term operation as an example. (C) SEM image of the pristine anode material (graphite). (D) BET analysis of the nitrogen adsorption–desorption isotherm, and pore size distribution curve (insert). (E) Irreversible growth of the H_2 concentration inside the battery with the cycle number. Point P_i (i = 1, 2, 3, 4) corresponds to point P_i in (A). (F) Schematic of the H_2 evolution pathway inside the battery cycled at low C rates, including H_2 initially adsorbed on the anode (blue circles), newly generated H_2 at the anode surface (yellow circles), Fickian diffusion (orange arrow), physical adsorption/desorption (blue arrow), and possible chemical reactions (R–H^+).

morphology of the anode material *via* SEM, which revealed a porous structure (Fig. 2C). This result suggests the excellent potential of this material for physical adsorption of H_2. Brunauer–Emmett–Teller (BET) surface area analysis was also performed to quantify the surface area and porosity of the anode material. The BET surface area is calculated as 2.32 $m^2\ g^{-1}$ using the data shown in Fig. 2D. The average pore size, found to be 28.67 nm from the desorption branch using the Barrett–Joyner–Halenda (BJH) method, is significantly larger than the H_2 diameter (0.29 nm), which allows the H_2 adsorption in these pores. These results confirm that the anode could play an important role in the reversible H_2 evolution through gas adsorption/desorption on/from its surface. We also validated the adsorption–desorption behaviour of H_2 in the graphite anode through an additional control experiment involving controlled heating and cooling of the battery (Fig. S13A and B, ESI†).

Apart from the reversible change of the H_2 evolution within batteries, an irreversible formation of H_2 was also observed.

We recorded the H_2 concentrations after 10 cycles at each C rate and full cooling down (points P_1–P_4 in Fig. 2A) and then plotted them against the cycle number (Fig. 2E). The H_2 concentration in the central void of the jelly roll increases with increasing cycle number and exhibits irreversible growth with increasing C rate. Because the physical adsorption/desorption equilibrium of H_2 in the electrode can be expected to remain the same for P_1 to P_4 under the same temperature and pressure conditions after the battery cools down, this irreversible formation of H_2 is most likely due to the chemical interactions that occur within the battery with increasing C rate. During charging and discharging, the graphite anode potential remains below the H^+/H_2 reduction potential, allowing for possible electrochemical H_2 generation. However, in commercial 18 650 batteries, the gas phase and SEI are already established during formation, and the dense SEI formed effectively inhibits H^+ reduction during routine cycling. As a result, the electrochemical generation of H_2 is minimal and results in the irreversible H_2 accumulation over time. We also conducted additional 10 charging–discharging cycles at a rate of 1C. After the battery cools down, the H_2 concentration is almost consistent with that at point P_4 (Fig. S13C and D, ESI†), further verifying that the reversible conversion is very likely caused by physical adsorption. Therefore, the H_2 evolution during normal cycling operation consists of reversible conversion due to physical adsorption/desorption on/from the electrode and irreversible formation due to chemical interactions that occur within the battery with increasing C rate.

In order to explain the experimental characteristics of H_2 evolution within batteries, the H_2 evolution mechanism, including chemical reactions, adsorption/desorption, Fickian diffusion (along the H_2 concentration gradient),[41] and thermal diffusion, is schematically proposed and depicted in Fig. 2F. In a fresh battery, a certain amount of H_2 may already exist both in the central void of the jelly roll and in the porous graphite electrode within the battery due to the battery formation.[42] In the charging/discharging stages with a low C rate, the electrode temperature gradually increases, resulting in H_2 desorption from the porous electrode and subsequent H_2 diffusion from the electrode to the central void of the jelly roll through Fickian diffusion. Similarly, when the temperature decreases in the open-circuit stage, H_2 diffuses back and is adsorbed on the porous electrode. This explains the reversible H_2 evolution with temperature. When the C rate is increased, the strong irreversible chemical formation of H_2 leads to a higher H_2 concentration level at the "End" stage of the process in Fig. 2F (P_1–P_4 of Fig. 2A). Our findings indicate that the H_2 concentration periodically changes along with the temperature in both reversible and irreversible manners when the battery cycles at low C rates.

NTC behaviour of the H_2 evolution within a battery

We further examined the special characteristics of the H_2 evolution at high C rate cycles. Fig. 3A depicts the transient variations in the temperature and H_2 concentration in the central void during one cycle at different C rates. The H_2 concentration is positively related with temperature at lower C rates, such as 1C and 2C, as explained above. However, interestingly, the H_2 evolution exhibits NTC behaviour at 3C and 4C, in which the H_2 concentration changes against temperature within certain charging–discharging stages, which are marked with "*" and "○" in Fig. 3A. At higher C rates, the internal peak temperature and its rise rate dramatically increase (Fig. 3B and C), respectively. This increase results in a greater temperature gradient between the electrodes and the central void and enables not only the abovementioned irreversible growth of the H_2 concentration but also likely amplified thermally induced mass diffusion, namely, Soret diffusion, of H_2 within the battery. Soret diffusion is the mass diffusion of molecules due to a temperature gradient, in which light molecules migrate opposite to the temperature gradient to increase their random kinetic energy.[30,43] Therefore, for the potential movement of H_2 from the cool region to the hot region within a battery (Fig. 3D), the Soret coefficient of H_2 is negative,[44] which leads to a H_2 evolution that is opposite to and competitive with that induced by Fickian diffusion.

A second H_2 evolution schematic with the thermal events that occur inside the battery at high C rates (3C and above) is depicted in Fig. 3E. The heating period of the battery during charge–discharge involves the following three stages. (i) Early stage: in the early stage of charging or discharging, the graphite anode is heated to a high temperature because of its low heat capacity,[45] with subsequent desorption of H_2 from its surface. The large H_2 concentration gradient between the anode surface and the central void enables marked Fickian diffusion to the central void, *i.e.*, the H_2 concentration increases. Note that Soret diffusion is a type of second-order mass diffusion and is generally weaker than Fickian diffusion. (ii) Middle stage: when the H_2 concentration in the central void of the battery approaches that on the anode surface, the Fickian diffusion induced by the concentration gradient becomes weak, whereas Soret diffusion of H_2 becomes dominant due to the large temperature gradient. This enables NTC behaviour of H_2 from the central void (low-temperature region) to the anode surface (high-temperature region), *i.e.*, the H_2 concentration in the central void decreases. (iii) Late stage: when the temperature of the central void approaches that of the anode surface, the temperature gradient becomes weak, reducing Soret diffusion. As a result, Fickian diffusion dominates H_2 transport again, and H_2 molecules migrate from the electrode surface to the central void again, *i.e.*, the H_2 concentration in the central void increases. The two key inflection points, P_1 and P_2, that separate these three stages are highlighted in Fig. 3A. During the cooling period of the battery in the open-circuit stage, three stages similar to those during charge–discharge occur. The experimental observation and proposed mechanism above reveal the H_2 evolution kinetics within battery cycles at high C rates.

Numerical and analytical solutions for the H_2 evolution regime diagram within batteries

To investigate the complicated H_2 evolution characteristics within batteries described above, we developed a 1D axisymmetric model for the H_2 evolution between the anode and electrolyte (Fig. 4A; see detailed descriptions in the Methods section and

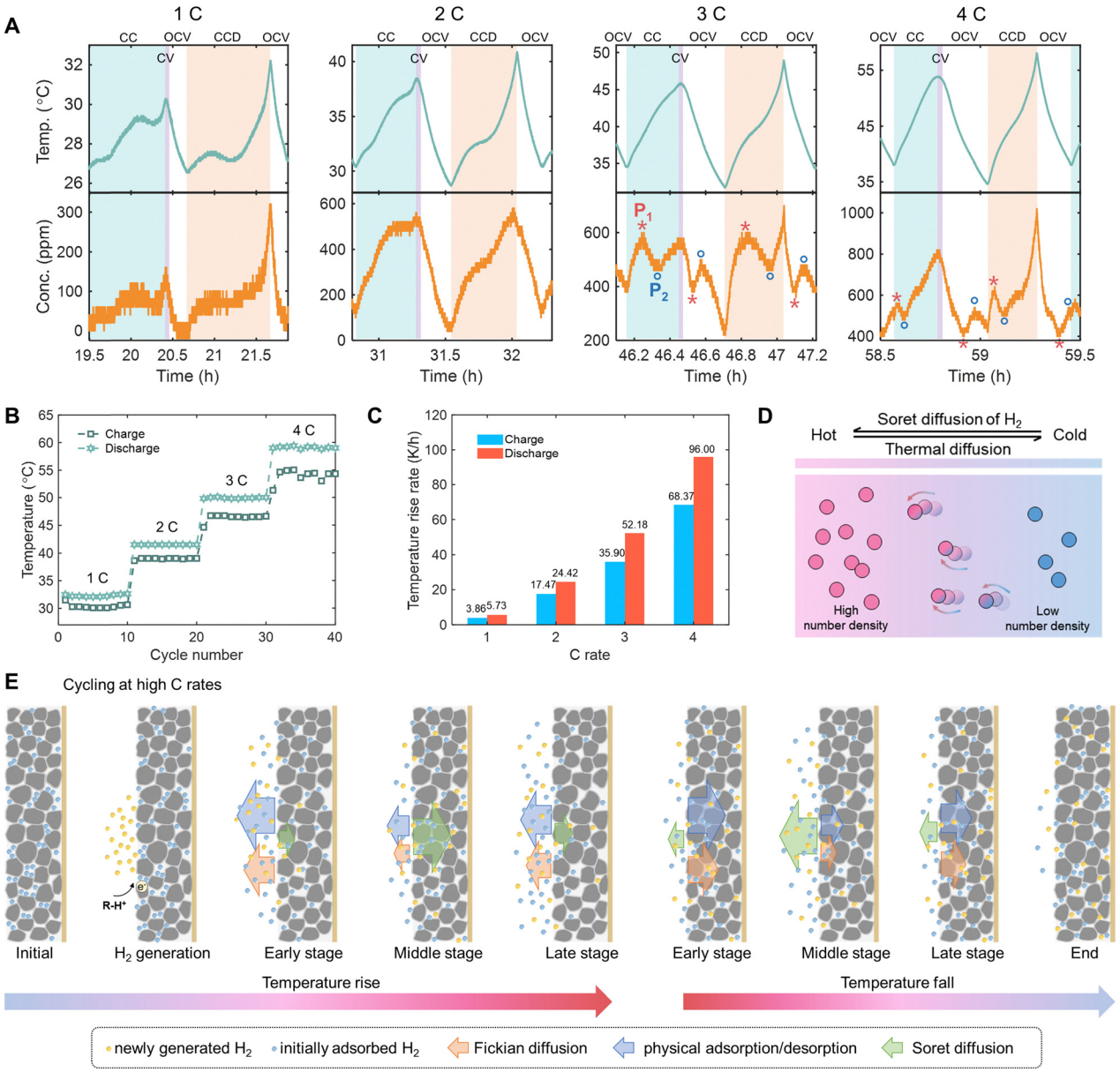

Fig. 3 NTC behaviour of the H_2 evolution kinetics inside the central void when the battery is cycled at high C rates. (A) Correspondence between the internal temperature (top) and C_{H_2} (bottom) at different C rates. (B) Maximum temperature during the charging stages (light green squares) and discharging stages (dark green hexagons) during long-term operation. (C) Internal temperature rise rates during charging–discharging cycling at different C rates. The internal temperature rise rates shown are obtained by averaging the values from 25 cycles. The temperature rise rates are simply calculated using the internal temperatures of the battery measured at the beginning and end of the charging (discharging) period. (D) Schematic diagram of the H_2 movement trajectory under Soret diffusion. (E) H_2 movement inside the battery during the temperature rise and temperature fall stages at high C rates, including H_2 initially adsorbed on the anode (blue circles), newly generated H_2 at the anode surface (yellow circles), Fickian diffusion (orange arrow), physical adsorption/desorption (blue arrow), Soret diffusion (green arrow), and possible chemical reactions ($R–H^+$).

Supplementary Text 1, ESI†). To simplify the analysis, a mixture of H_2 and electrolyte solvents is considered here, and the jelly roll is treated as a homogenous porous interface with a uniform concentration of H_2 (C_{ele}) and a uniform temperature (T_{ele}). Thermal diffusion, Fickian diffusion of H_2, and Soret diffusion of H_2 in the electrolyte are considered in the transient species and energy governing equations below (eqn (1) and (2)). The Langmuir adsorption equation[46] is employed to describe the H_2 adsorption and desorption at the anode interface. The H_2 concentration C_{ele} and temperature T_{ele} in the jelly roll are controlled by H_2 adsorption/desorption and the Joule heating rate (k), respectively, whereas the C_{cv} and T_{cv} in the central void are both functions of the radial distance to the anode (r) and time (t). Based on the continuity of these functions in space, at the electrode boundary with a radius of R, $C_{ele} = C_{cv,r=R}$, and $T_{ele} = T_{cv,r=R}$. Central finite difference approximations are employed to solve the governing equations given below. A detailed description of the governing equation constructions is presented in Supplementary Text 1

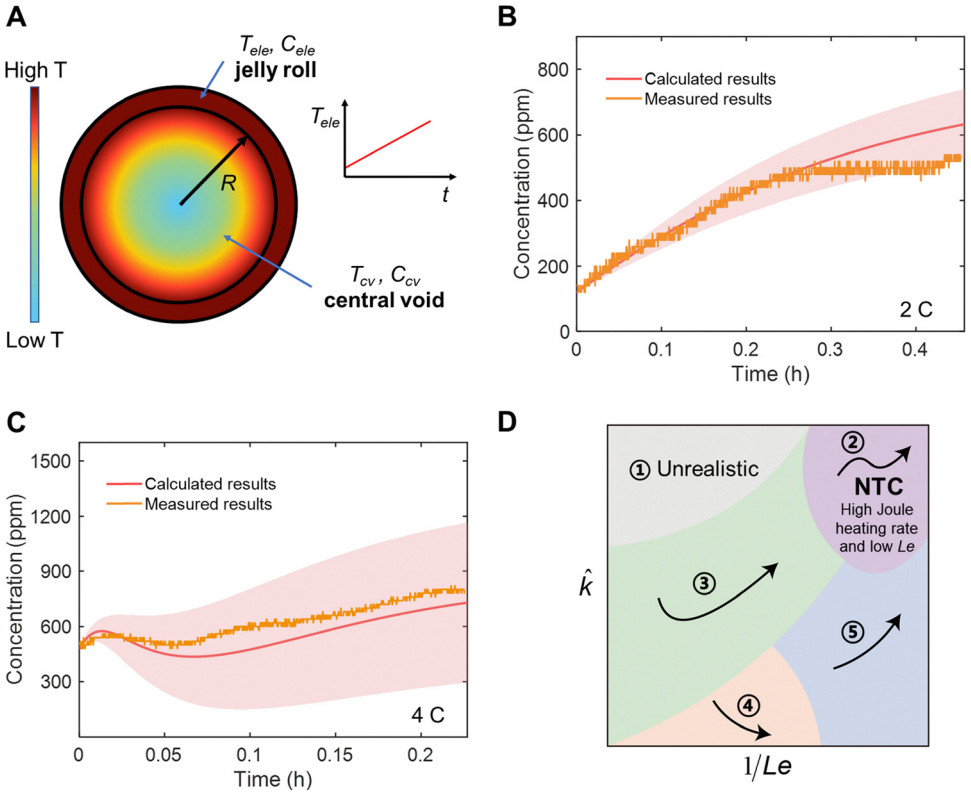

Fig. 4 H_2 evolution kinetics inside the central void. (A) Simplified model of the battery internal thermal process, where the jelly roll is treated as a unified entity with a uniform temperature (T_{ele}), and the adsorbed H_2 is evenly distributed within it with a certain concentration (C_{ele}). The T_{ele} is assumed to increase linearly with time (t). (B) and (C) Calculated and measured results of the H_2 evolution during charging at 2C and 4C, respectively, with the Joule heating rate set to remain constant in the calculations. (D) Regime diagram for the H_2 evolution within a battery in $\hat{k}$ and 1/Le space. The arrows indicate the change in the H_2 concentration with increasing temperature, and the numbers represent the regions with different H_2 evolution behaviours.

(ESI†), and the transport parameters and their uncertainties are provided in Tables S2 and S3 (ESI†).

$$\rho c_p \frac{\partial T_{cv}}{\partial t} = \lambda \nabla^2 T_{cv} \quad (1)$$

$$\frac{\partial Y_m}{\partial t} = D_m \nabla^2 Y_m + D_m S_{T,m} \nabla^2 T_{cv} \quad (2)$$

where ρ, c_p, T, and λ represent the density, specific heat capacity, temperature, and thermal conductivity of the mixture, respectively; Y_m, D_m, and $S_{T,m}$ represent the mass fraction, Fickian diffusivity, and Soret coefficient of substance m, respectively.

The numerically predicted H_2 concentration curves in the center of the central void with including Soret diffusion for 2C and 4C charging processes are plotted with error bars (due to transport data uncertainties) in Fig. 4B and C. The experimental results of the H_2 concentration fall within the error bars of the predicted H_2 evolution curves, which indicates a high consistency between the numerical solution and the *operando* measurements. We also performed the numerical calculation without the Soret diffusion and plotted the H_2 concentration curves (Fig. S14, ESI†). It is seen the predicted curve is away from the experimental results markedly and the NTC behaviour is not captured at the 4C cycle, where Soret diffusion is as important as Fickian diffusion.

To further understand the NTC behaviour of H_2, we analytically solved the transient governing equations of H_2 evolution (eqn (1) and (2)) during the charging period (see details in the Methods section and Supplementary Text 2, ESI†). The evolution of the dimensionless temperature and concentration of H_2 in the center of the central void (r = 0), *i.e.*, $\hat{t}_{cv,r=0}$ and $\hat{C}_{cv,r=0}$, with t is given by

$$\widehat{T}_{cv,r=0} = 1 + \widehat{kt} - \sum_{n=1}^{+\infty} \frac{2\widehat{k}\left\{1 - \exp\left[-\left(x_n^{(0)}\right)^2 \widehat{t}\right]\right\}}{\left[x_n^{(0)}\right]^3 \left[J_1\left(x_n^{(0)}\right)\right]} \quad (3)$$

where β is a dimensionless number reflecting the strength of the desorption effect on the H_2 concentration at the surface of the electrode, and is affected by the BET surface area, Le is the Lewis number defined as the ratio of thermal diffusivity to mass diffusivity, and can be expressed as Le = $\lambda/(\rho \times C_p \times D)$, where λ, ρ, C_p, and D denote thermal conductivity, density, specific heat capacity, and mixture-averaged diffusion coefficient, respectively, and S_r is the Soret number given by $S_r = S_T \times Y/T$. Additionally, $\hat{k}$, E_d, T_0, R_0, and $\hat{t}$ represent the dimensionless Joule heating rate, desorption activation energy, initial temperature, ideal gas constant, and dimensionless time, respectively (a detailed description is provided in

$$\hat{C}_{\mathrm{cv},r=0} = \frac{1-\beta\exp\left(-\left(\hat{k}E_\mathrm{d}/R_0T_0\right)\hat{t}\right)}{1-\beta} + \sum_{n=1}^{+\infty}\left\{\begin{array}{l}\dfrac{2\beta\hat{k}}{1-\beta}\dfrac{\exp\left(-\left(x_n^{(0)}\right)^2\hat{t}/\mathrm{Le}\right)-\exp\left(-\left(\hat{k}E_\mathrm{d}/R_0T_0\right)\hat{t}\right)}{\left[x_n^{(0)}\right]\left[J_1\left(x_n^{(0)}\right)\right]\left(E_\mathrm{d}\left[x_n^{(0)}\right]^2\Big/R_0T_0\mathrm{Le}-\hat{k}\right)} \\ +\dfrac{2\hat{k}S_\mathrm{r}\left\{1-\mathrm{Le}+\mathrm{Le}\exp\left[-\left(x_n^{(0)}\right)^2\hat{t}\Big/\mathrm{Le}\right]-\exp\left[-\left(x_n^{(0)}\right)^2\hat{t}\right]\right\}}{\left[x_n^{(0)}\right]^3\left[J_1\left(x_n^{(0)}\right)\right](1-\mathrm{Le})}\end{array}\right\} \quad (4)$$

Supplementary Text 2, ESI†). $J_n(x)$ is the nth-order Bessel function, with $x_n^{(0)}$ as the nth root of $J_0(x) = 0$.

The analytical solution of the H_2 evolution rate in eqn (4) is a function of t, $\hat{k}$, Le, β, E_d, and S_r, where $\hat{k}$ and Le are two major variables for the H_2 evolution in battery operations. Therefore, we plotted the H_2 evolution regime diagram in a $\hat{k}$ and 1/Le space, and divided it into five regions (Fig. 4D; see details in Supplementary Text 2, ESI†). Region (1) generally involves an extremely high $\hat{k}$, over a million times E_d/R_0T_0, which is unrealistic for practical battery cycles. Region (2) corresponds to a high $\hat{k}$ and a low Le. A high $\hat{k}$ represents a high temperature and a high H_2 concentration from desorption on the anode surface, leading to high thermal and concentration gradients between the anode and electrolyte. A low Le indicates slow thermal diffusion and fast Fickian diffusion. In the early stage of the charging–discharging cycle (Fig. 3E), a large amount of H_2 desorbs from the anode due to the high Joule heating rate and rapidly diffuses into the central void due to the fast Fickian diffusion associated with a low Le; meanwhile, the slow thermal diffusion suppresses Soret diffusion. This results in an increase in the H_2 concentration in the central void with fast Fickian diffusion and slow Soret diffusion. In the middle stage, the H_2 concentration gradient between the anode and electrolyte decreases while the thermal gradient remains high because the thermal diffusion is slower at a low Le, so the Soret diffusion (induced by the thermal gradient) exceeds the Fickian diffusion (induced by the concentration gradient). This results in a decrease in the H_2 concentration in the central void with t. As $T_{\mathrm{cv},r=0}$ is positively correlated with t, the H_2 evolution exhibits NTC behaviour. In the late stage, Soret diffusion also markedly slows because of the quasi-uniform temperature distribution between the anode and electrolyte, and Fickian diffusion becomes dominant again. This causes a further increase in the H_2 concentration in the central void. The experimental results of H_2 evolution when the battery cycled under 3C and 4C in Fig. 3A fall into this region.

Regions (3) and (4) correspond to a low to medium $\hat{k}$ and a high Le. In the early stage, the H_2 concentration in the central void decreases because of the fast Soret diffusion and slow Fickian diffusion at a high Le in both regions (3) and (4). However, the Fickian diffusion in region (3) is relatively fast compared to that in region (4), as the former maintains a higher $\hat{k}$ with the higher H_2 concentration gradient between the anode and electrolyte. Therefore, in the later stage, the H_2 concentration increases in region (3) but continues to decrease in region (4). We observed the H_2 evolution behaviours for the other battery in regions (3) and (4) at 2C and 1C, respectively (Fig. S15B, ESI†). Region (5) corresponds to a low $\hat{k}$ and a low Le, where Fickian diffusion is much faster than Soret diffusion. As a result, the H_2 concentration increases with time or temperature. Therefore, the diagram of H_2 evolution above summarizes the different H_2 evolution characteristics that may occur in the battery cycles with different battery structures and operation conditions. The experimental results of H_2 evolution when the battery cycled under 1C and 2C in Fig. 3A fall into this region.

The distinct H_2 evolution behaviours in different 18 650 batteries are likely due to the different physical structures and internal chemical environments associated with Le, BET surface area (Fig. S15, ESI†). Overall, the comprehensive H_2 evolution kinetics within a battery was numerically and analytically computed, which well explains the NTC behaviour observed in the experiment. In particular, the NTC H_2 behaviour predicted for a high C rate (high $\hat{k}$) and a low Le within a battery, represented by region (2), is experimentally observed. Finally, these results revealed the H_2 evolution mechanisms within a lithium-ion battery and imply a potential strategy to adjust the H_2 evolution behaviour in batteries through optimized design of the battery structure and charging–discharging strategies.

Safety-oriented battery design strategies

The analysis above indicates that H_2 accumulation within the battery can be suppressed *via* the NTC behaviour. Therefore, we further elucidated the H_2 evolution characteristics during the battery thermal runaway process using the numerical computation above. Under externally triggered failure scenarios (*e.g.*, mechanical puncture or thermal abuse), a significant heating rate exists and triggers thermal runaway. It is seen from Fig. 5A that the H_2 accumulations before and after the thermal runaway excluding the NTC behaviour are respectively around 2 and 3 times that with the NTC behaviour. This strongly suggests that the structural optimization and charging–discharging strategies enhancing Soret diffusion and NTC behaviour of H_2 could effectively mitigate severe thermal runaway risks and advance safety-oriented battery engineering.

In order to guide the safety-oriented battery design, we further decoded the influence of the Joule heating rate, Lewis number, and BET surface area on the H_2 growth in the central void region of the battery during charging–discharging cycles in Fig. 5B–E. For LFP batteries, the typical value ranges of these

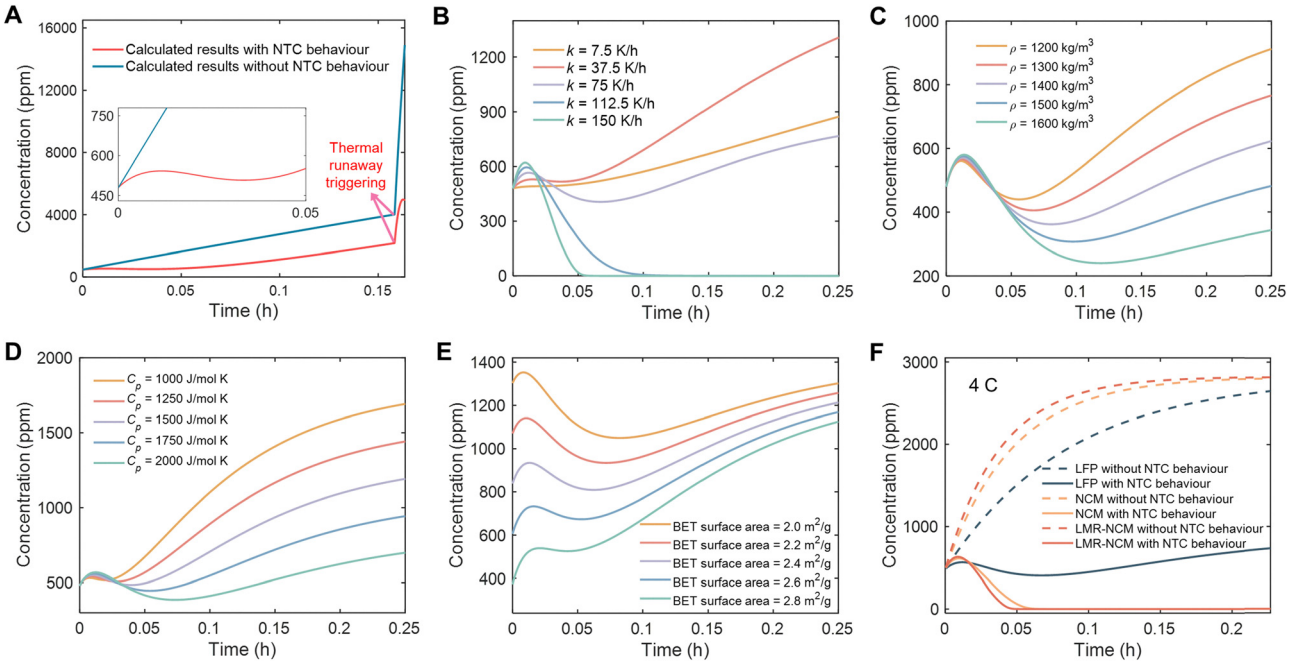

Fig. 5 NTC behaviour-driven strategies for enhancing battery safety. (A) The trend of H_2 concentration within the battery before and after thermal runaway, where the simulative thermal runaway is triggered by a prompt temperature rise of 2.4 K s^{-1} from scenarios such as puncture or thermal abuse. (B)–(E) The influence of different characteristic parameters on the NTC behaviour, which includes the Joule heating rate (B), the density (C) and specific heat capacity (D) of the electrolyte, and the BET surface area (E). (F) Comparison of H_2 evolution during charging at 4C within batteries with different energy densities, with and without consideration of the NTC behaviour.

key parameters are listed in Table S4 (ESI†). First, the NTC behaviour is significantly enhanced with a low H_2 concentration under aggressive high heating rate cycling conditions (Fig. 5B), where H_2 is confined within the graphite anode. It potentially establishes a critical safety paradigm for next-generation smart battery architectures. Second, Lewis number, a measure of the ratio of thermal and mass diffusions, is suggested to be reduced by designing an electrolyte mixture with higher density and heat capacity for amplifying the NTC behaviour and lowering the H_2 concentration within a battery. This has been validated in our numerical simulations in Fig. 5C and D. The BET surface area affects the porosity of the graphite anode, where a larger surface area improves the H_2 adsorption capability. This results in increased H_2 retention within the anode, thereby lowering the overall H_2 concentration inside the battery during cycling (Fig. 5E). Therefore, optimizing the electrolyte composition and electrode material design can effectively suppress the accumulation of H_2 during cycling, wherein Soret diffusion dominates over Fickian diffusion and desorption from the anode surface. This could potentially reduce the risk of thermal runaway and battery explosion.

We also examined our H_2 evolution theory for high-energy-density lithium-ion batteries such as NCM batteries and LMR-NCM batteries. They typically exhibit much faster temperature rise rates than LFP batteries during cycling. Their thermal characteristics and charging conditions are summarized in Table S5 (ESI†). We mimicked their different Joule heating rates under 4C conditions in the simulation and plotted the H_2 concentration with and without including the NTC behaviour in Fig. 5F. The H_2 growth in the central void is highly inhibited with the inclusion of NTC behaviour. Therefore, by effective optimization of the charging/discharging strategy, the thermal runaway risk through "temperature rise → H_2 release → combustion/explosion" in high-energy-density batteries may be highly mitigated. As such, the H_2 growth within a battery could be inhibited by guiding the battery design on the electrolyte and anode and optimizing cycling strategies in terms of the Joule heating rate.

Conclusions

The formation of H_2 during battery cycling is strongly related to cathode degradation, heat release, battery thermal runaway, and even the risk of fire and explosion, which is closely linked to its safe operation. However, an explicit and detailed mechanism is still unknown as the time-resolved *operando* quantification approach is significantly lacking during charging–discharging cycles within batteries. In this work, we quantified the H_2 evolution inside a commercial 18 650 battery during cycling *via* a novel *operando* method based on an *in situ* FBG sensor with compact size, high sensitivity, and long-term reliability. Time-resolved H_2 reversible adsorption/desorption and irreversible formation inside the battery were observed to be associated with the temperature during charging–discharging cycles for the first time. We observed reversible H_2 adsorption/desorption up to 380 ppm at 1C and up to 1040 ppm at 4C, as well as irreversible H_2 formation up to

220 ppm after long-term cycling. Moreover, we discovered that the H_2 exhibits unique NTC behaviour at high heating rates during battery cycling in experiments.

A comprehensive theory of the transient and spatial evolution of H_2 inside batteries including adsorption/desorption, Fickian diffusion, Soret diffusion, and chemical reactions was developed and applied to explain the H_2 evolution characteristics. The numerical solution predicts the NTC behaviour of H_2 observed in experiments with excellent agreements, and the analytical solution reveals that the NTC behaviour of H_2 comes from the enhanced Soret diffusion of H_2 at a high Joule heating rate and a low Lewis number within batteries. A regime diagram for the H_2 evolution within batteries in a $\hat{k}$ and 1/Le space is also provided. Moreover, the present H_2 evolution theory has also been validated for thermal runaway and for high-energy-density batteries in numerical simulations, where the H_2 growth could be highly inhibited with the inclusion of NTC behaviour. It also provides approaches to suppress the H_2 growth by amplifying the NTC behaviour through (i) higher Joule heating rate, (ii) a lower Le of electrolytes, or (iii) employing a suitable porous anode material for reversible H_2 adsorption. The present study provides theoretical guidance for the high-safety battery design and alleviates anxiety toward the risk of thermal runaway and explosive accidents during high C rate cycles of high-energy-density batteries.

It should be noted that only the electrolyte and H_2 were considered as the key components within batteries, while fluid convection, thermal expansion, and molecular viscosity were neglected. Future study needs to incorporate more gas and liquid components, and employ governing equations with the chemical term in detail for revealing the irreversible H_2 formation within batteries. Meanwhile, while the proposed 1D axisymmetric model and regime diagram offer useful qualitative insight, their predictive accuracy may be limited in scenarios with strong spatial heterogeneities in porosity, temperature, or gas generation profiles. The regime boundaries are not absolute but should be interpreted as trend indicators within an idealized geometry. For real commercial batteries, further refinement through 2D or 3D modeling and experimental validation will be necessary.

Overall, the present study provides novel insight into the H_2 evolution in batteries through an advanced fiber optic approach and a comprehensive analytical theory. This study represents a key discovery for applying the present diagnostic and theoretical approaches to understand the *operando* and time-resolved evolution of other crucial gaseous species and their interactions with electrodes and electrolytes associated with thermal runaway within batteries.

Author contributions

Y. W., H. Z. and D. X. conceived and designed the research project. Y. W. and G. M. performed the design of the FBG sensor. Y. W. and Y. G. performed the fabrication of the FBG sensor and the experiments on lithium-ion batteries. Y. W., Y. G., S. G., H. Z. and D. X. analysed the data. S. G. and P. Z. performed the calculations of H_2 evolution. All the authors discussed the data and wrote the paper.

Conflicts of interest

There are no conflicts to declare.

Data availability

The data supporting this article have been included as part of the ESI.†

Acknowledgements

This work was supported by MOST (2022YFB2502100 and 2023YFE0120900), NSFC (52130202, 52222706 and 22361132538), APRC (9610601) and China Postdoctoral Science Foundation (GZC20230045). We thank Dr Quanquan Pang from the School of Materials Science and Engineering, Peking University, for reading and editing the paper.

Notes and references

1 M. Armand and J.-M. Tarascon, *Nature*, 2008, **451**, 652–657.
2 J.-M. Tarascon and M. Armand, *Nature*, 2001, **414**, 359–367.
3 X. Feng, D. Ren, X. He and M. Ouyang, *Joule*, 2020, **4**, 743–770.
4 G. Harper, R. Sommerville, E. Kendrick, L. Driscoll, P. Slater, R. Stolkin, A. Walton, P. Christensen, O. Heidrich and S. Lambert, *Nature*, 2019, **575**, 75–86.
5 G. Crabtree, *Science*, 2019, **366**, 422–424.
6 Y. Wang, X. Feng, Y. Peng, F. Zhang, D. Ren, X. Liu, L. Lu, Y. Nitta, L. Wang and M. Ouyang, *Joule*, 2022, **6**, 2810–2820.
7 S. Yuan, C. Chang, J. Zhang, Y. Liu and X. Qian, *J. Loss Prev. Process Ind.*, 2022, **79**, 104816.
8 H. Xiao, Q. Duan and J. Sun, *Renewable Sustainable Energy Rev.*, 2018, **81**, 1988–2001.
9 C. R. Lee, H. Y. Jang, H. J. Leem, M. A. Lee, W. Kim, J. Kim, J. H. Song, J. Yu, J. Mun and S. Back, *Adv. Energy Mater.*, 2024, **14**, 2302906.
10 Q. Yin, Y. Duan, J. Du, H. Zhang, Q. Fu, X. Yang and X. Li, *Adv. Mater.*, 2025, 2502077.
11 Y. Jin, Z. Zheng, D. Wei, X. Jiang, H. Lu, L. Sun, F. Tao, D. Guo, Y. Liu and J. Gao, *Joule*, 2020, **4**, 1714–1729.
12 N. Galushkin, N. Yazvinskaya and D. Galushkin, *J. Electrochem. Soc.*, 2019, **166**, A897.
13 H. Zhang, J. Chen, B. Zhang, X. Wu, Z. Li, L. Chen, J. Wang, X. Yu, H. Luo and J. Xue, *J. Energy Chem.*, 2023, **84**, 286–291.
14 R. Lundström and E. J. Berg, *J. Power Sources*, 2021, **485**, 229347.
15 F. Larsson, P. Andersson, P. Blomqvist and B.-E. Mellander, *Sci. Rep.*, 2017, **7**, 10018.
16 S. Bertilsson, F. Larsson, M. Furlani, I. Albinsson and B.-E. Mellander, *J. Power Sources*, 2017, **365**, 446–455.

17 L. Pang, H. Li, X. Feng, Z. Zhao, C. Ouyang and Z. Peng, *ACS Energy Lett.*, 2024, **9**, 3587–3594.
18 Q. Meng, Y. Huang, L. Li, F. Wu and R. Chen, *Joule*, 2024, **8**, 344–373.
19 J. Huang, S. T. Boles and J.-M. Tarascon, *Nat. Sustainability*, 2022, **5**, 194–204.
20 W. Wang, Y. Zhang, B. Xie, L. Huang, S. Dong, G. Xu and G. Cui, *Adv. Energy Mater.*, 2024, 2304173.
21 G. Yang, C. Leitão, Y. Li, J. Pinto and X. Jiang, *Measurement*, 2013, **46**, 3166–3172.
22 J. Huang, L. Albero Blanquer, J. Bonefacino, E. R. Logan, D. Alves Dalla Corte, C. Delacourt, B. M. Gallant, S. T. Boles, J. Dahn and H.-Y. Tam, *Nat. Energy*, 2020, **5**, 674–683.
23 W. Mei, Z. Liu, C. Wang, C. Wu, Y. Liu, P. Liu, X. Xia, X. Xue, X. Han and J. Sun, *Nat. Commun.*, 2023, **14**, 5251.
24 R. Wang, H. Zhang, Q. Liu, F. Liu, X. Han, X. Liu, K. Li, G. Xiao, J. Albert and X. Lu, *Nat. Commun.*, 2022, **13**, 547.
25 J. Huang, X. Han, F. Liu, C. Gervillié, L. A. Blanquer, T. Guo and J.-M. Tarascon, *Energy Environ. Sci.*, 2021, **14**, 6464–6475.
26 F. Liu, W. Lu, J. Huang, V. Pimenta, S. Boles, R. Demir-Cakan and J.-M. Tarascon, *Nat. Commun.*, 2023, **14**, 7350.
27 E. Miele, W. M. Dose, I. Manyakin, M. H. Frosz, Z. Ruff, M. F. De Volder, C. P. Grey, J. J. Baumberg and T. G. Euser, *Nat. Commun.*, 2022, **13**, 1651.
28 C. Gervillié-Mouravieff, C. Boussard-Plédel, J. Huang, C. Leau, L. A. Blanquer, M. B. Yahia, M.-L. Doublet, S. Boles, X. Zhang and J. Adam, *Nat. Energy*, 2022, **7**, 1157–1169.
29 A. Ghannoum, P. Nieva, A. Yu and A. Khajepour, *ACS Appl. Mater. Interfaces*, 2017, **9**, 41284–41290.
30 C. K. Law, *Combustion physics*, Cambridge University Press, 2010.
31 A. Fick, *J. Membr. Sci.*, 1995, **100**, 33–38.
32 G. Ma, Y. Wang, W. Qin, H. Zhou, C. Yan, J. Jiang and Y. Ju, *High Voltage*, 2021, **6**, 367–386.
33 A. D. Kersey, M. A. Davis, H. J. Patrick, M. LeBlanc, K. P. Koo, C. G. Askins, M. A. Putnam and E. J. Friebele, *J. Light Technol.*, 1997, **15**, 1442–1463.
34 T. B. Flanagan and W. Oates, *Annu. Rev. Mater. Sci.*, 1991, **21**, 269–304.
35 H. Conrad, G. Ertl and E. Latta, *Surf. Sci.*, 1974, **41**, 435–446.
36 G. Wang, J. Dai and M. Yang, *IEEE Sens. J.*, 2020, **21**, 12706–12718.
37 P. J. Bugryniec, J. N. Davidson, D. J. Cumming and S. F. Brown, *J. Power Sources*, 2019, **414**, 557–568.
38 M. Metzger, B. Strehle, S. Solchenbach and H. A. Gasteiger, *J. Electrochem. Soc.*, 2016, **163**, A798.
39 D. P. Broom and D. P. Broom, *Hydrogen Storage Materials: The Characterisation of Their Storage Properties*, 2011, pp. 19–59.
40 X. Deng, Y. Huang, Y. Han, J. Du, J. Tian, Y. Li, Y. Yu, Y. Shen and Y. Huang, *Angew. Chem., Int. Ed.*, 2024, e202412222.
41 E. L. Cussler, *Diffusion: mass transfer in fluid systems*, Cambridge University Press, 2009.
42 J. Scharf, C. von Lüders, F.-M. Matysik, C. Misiewicz, J. Wandt and E. J. Berg, *J. Power Sources*, 2024, **603**, 234419.
43 M. Rahman and M. Saghir, *Int. J. Heat Mass Transfer*, 2014, **73**, 693–705.
44 J. F. Grcar, J. B. Bell and M. S. Day, *Proc. Combust. Inst.*, 2009, **32**, 1173–1180.
45 M. Steinhardt, J. V. Barreras, H. Ruan, B. Wu, G. J. Offer and A. Jossen, *J. Power Sources*, 2022, **522**, 230829.
46 I. Langmuir, *Phys. Rev.*, 1916, **8**, 149.